

Liquid demixing in elastic networks: cavitation, permeation, or size selection?

Pierre Ronceray,^{1,2,*} Sheng Mao,^{3,4} Andrej Košmrlj,^{4,5} and Mikko P. Haataja^{4,5,†}

¹Center for the Physics of Biological Function, Princeton University, Princeton, New Jersey 08544, USA

²Aix Marseille Univ, Université de Toulon, CNRS, CPT,
Turing Center for Living Systems, Marseille, France

³Department of Mechanics and Engineering Science, BIC-ESAT,
College of Engineering, Peking University, Beijing 100871, People's Republic of China

⁴Department of Mechanical and Aerospace Engineering,
Princeton University, Princeton, New Jersey 08544, USA

⁵Princeton Institute for the Science and Technology of Materials (PRISM),
Princeton University, Princeton, New Jersey 08544, USA

Demixing of multicomponent biomolecular systems via liquid-liquid phase separation (LLPS) has emerged as a potentially unifying mechanism governing the formation of several membraneless intracellular organelles (“condensates”) [1–7], both in the cytoplasm (*e.g.*, stress granules) and in the nucleoplasm (*e.g.*, nucleoli). While both *in vivo* experiments [8] and studies of synthetic systems [9, 10] demonstrate that LLPS is strongly affected by the presence of a macromolecular elastic network, a fundamental understanding of the role of such networks on LLPS is still lacking. Here we show that, upon accounting for capillary forces responsible for network expulsion, small-scale heterogeneity of the network, and its nonlinear mechanical properties, an intriguing picture of LLPS emerges. Specifically, we predict that, in addition to the experimentally observed cavitated droplets [8, 9] which fully exclude the network, two other phases are thermodynamically possible: elastically arrested, size-limited droplets at the network pore scale, and network-including macroscopic droplets. In particular, pore size-limited droplets may emerge in chromatin networks, with implications for structure and function of nucleoplasmic condensates.

When LLPS occurs without mechanical constraints (Fig. 1A), the thermodynamically stable outcome of the demixing is a macroscopic spherical droplet of the minority liquid (red) embedded within the majority phase (yellow). This ensures that the contact surface per droplet volume between the two liquids is minimized, and results in a negligible, sub-extensive free energy penalty compared to the bulk phase-separated liquid. In the presence of an elastic matrix hindering LLPS, in contrast, we distinguish and study here three distinct scenarios by which demixing can occur (Fig. 1B). Each scenario results in a specific free energy cost compared to the reference, unhindered case: (i) The minority liquid can create a macroscopic cavity, which incurs a deformation

energy penalty E_{el} associated with the elastic matrix. (ii) Alternatively, the minority liquid may form an extensive number of microdroplets fitting within the pores of the network, which avoids elastic deformation but incurs an extensive surface energy penalty E_{surf} . (iii) Finally, rather than fully excluding the network, the minority droplet can permeate through it, resulting in a finite wetting energy E_{wet} between the droplet and the network. Below, we establish an equilibrium phase diagram for LLPS within an elastic network by assessing the relative thermodynamic stability of each scenario.

Specifically, we introduce physically-based models for each of the three energy penalties compared to the reference situation of demixing in the absence of a network (Fig. 1A), and evaluate the stability of each phase by quantifying this free energy cost per volume of phase-separated minority liquid, an approach previously used fruitfully in the context of block copolymer phase behavior [11]. We focus on identifying the thermodynamically stable droplet configurations, and thus ignore all kinetic processes (incl. nucleation, growth and coarsening). In addition, we assume that the droplets occupy a negligible volume fraction, and hence neglect all elastic and chemical inter-droplet interactions. We first employ simple scaling arguments to establish a morphological phase

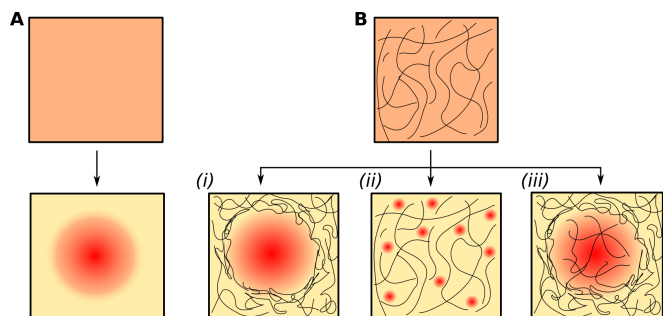


FIG. 1. **A.** Liquid-liquid phase separation (LLPS) from an initially mixed phase (*top*) results in a macroscopic droplet of the red minority liquid immersed in the yellow majority one (*bottom*). **B.** When LLPS occurs with the initial mixed phase imbedded in an elastic network (*top*), we identify three possible outcomes (*bottom*): (i) Cavitation. (ii) Microscale droplets. (iii) Permeation of the network into the minority phase.

* pierre.ronceray@univ-amu.fr

† mhaataja@princeton.edu

diagram by considering only the dominant term(s) of the free energy for each phase. Motivated by existing theoretical approaches [9, 10, 12, 13], we then develop a comprehensive theory of droplets constrained by elastic networks by accounting for capillary forces responsible for network expulsion from droplets, as well as heterogeneities in the network structure and its nonlinear mechanical properties. Both analytical and numerical approaches are employed to confirm the salient features of the phase diagram and elucidate the nature of phase transitions between the droplet phases.

We begin by considering scenario (i), where a macroscopic droplet of size $r \rightarrow \infty$ forms by creating a network-excluding cavity. This scenario was previously considered for *in vitro* oil-water mixtures in silicone gels [9, 10, 12] and *in vivo* droplets in the cell nucleus [8]. In order to form a macroscopic cavity from an initial pore, large deformations must occur in the network. Therefore, it is necessary to go beyond simple linear elasticity in the treatment of the network mechanics. The simplest such extension is a neo-Hookean (NH) constitutive relation, considered in Refs. [8–10], where the elastic energy

$$E_{\text{el}}(r) \sim \frac{4\pi r^3}{3} \alpha G \quad (1)$$

scales as the volume of the cavity when $r \rightarrow \infty$. Here, G denotes the shear modulus of the network, while the numerical coefficient $\alpha \sim \frac{5}{2}$ is a material parameter. This simple behavior reasonably describes a broad class of artificial gels [14], and several mechanisms can lead to such a volume scaling, such as detachment of cross-links or fracture at fixed hoop stress [15, 16]. For this scenario, the free energy per volume penalty compared to the reference system without a network is thus

$$\Delta g_{(i)} \sim \alpha G. \quad (2)$$

This constant free energy penalty results in a shift of the phase boundary to lower temperatures. Remarkably, this behavior was characterized and validated for *in vitro* systems [9], with a value $\alpha \approx 1.5$. In the presence of macroscopic gradients in the network stiffness, Eq. (2) also implies that droplet growth is favored in softer regions of the system, where the phase-separated liquid has a lower free energy [8, 10, 17, 18].

While this model captures the macroscopic elastic response of the material, it does not account for small-scale heterogeneities. In both biological and artificial systems considered here, the elastic network is constituted by polymers with a finite pore size ξ characterizing the size of interstices between polymers. Consider now scenario (ii) in Fig. 1B, in which microdroplets with $r = \xi$ form within these pores without deforming the network. In this case, $E_{\text{el}} = 0$, while due to their small size, the droplets incur a substantial surface energy penalty $E_{\text{surf}} = 4\pi\xi^2\gamma$, where γ denotes the surface tension between the two liquid phases. Per volume of the minority

species, this result in a free energy penalty

$$\Delta g_{(ii)} \sim \frac{3\gamma}{\xi} \quad (3)$$

for scenario (ii), compared to our reference system in absence of elastic network. Comparing Eqs. (3) and (2) reveals that in such a porous network, the trade-off between elastic and surface energy is controlled by the *elasto-capillary number* [19]:

$$h \equiv \frac{3\gamma}{\xi G}. \quad (4)$$

When $h > \alpha$, *i.e.*, for an elastically homogeneous network and large liquid-liquid surface tension, scenario (i) is thermodynamically favored, leading to the formation of macroscopic cavitated droplets. In contrast, when $h < \alpha$, pore-size-limited microdroplets corresponding to scenario (ii) are thermodynamically more stable (Fig. 2).

In the scenarios considered thus far, the network is fully excluded from the droplets. We now consider scenario (iii) from Fig. 1B: the partial inclusion of the network in macroscopic droplets of the minority phase. To assess the stability of this scenario, we introduce a wetting energy E_{wet} , emanating from the minority phase permeating through the network, as

$$E_{\text{wet}} = \frac{4\pi r^3}{3} (1 - \varphi) \sigma_p, \quad (5)$$

where φ denotes the fraction of network expelled from the droplet compared to the undeformed state, and σ_p denotes the *permeation stress*. Microscopically, σ_p arises from differential wetting energy per unit length of filaments constituting the network in contact with the two fluids [20] (see SI Sec. E). Eq. (5) translates this microscopic wetting phenomenon into a macroscopic effect, which results in a stress discontinuity at the liquid-liquid

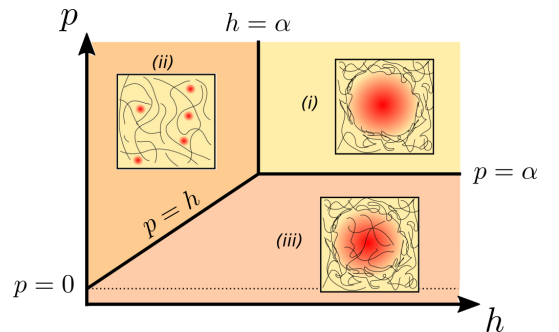


FIG. 2. Putative phase diagram from simple scaling arguments, indicating the most stable state for liquid-liquid phase separation in an elastic network, as a function of the elasto-capillary number h (Eq. (4)) and the permeo-elastic number p (Eq. (7)). Note that only the dominant contribution to the free energy is retained here, corresponding to Eqs. (2), (3) and (6), respectively for the cavitated (i), micro-droplets (ii) and permeated (iii) phases.

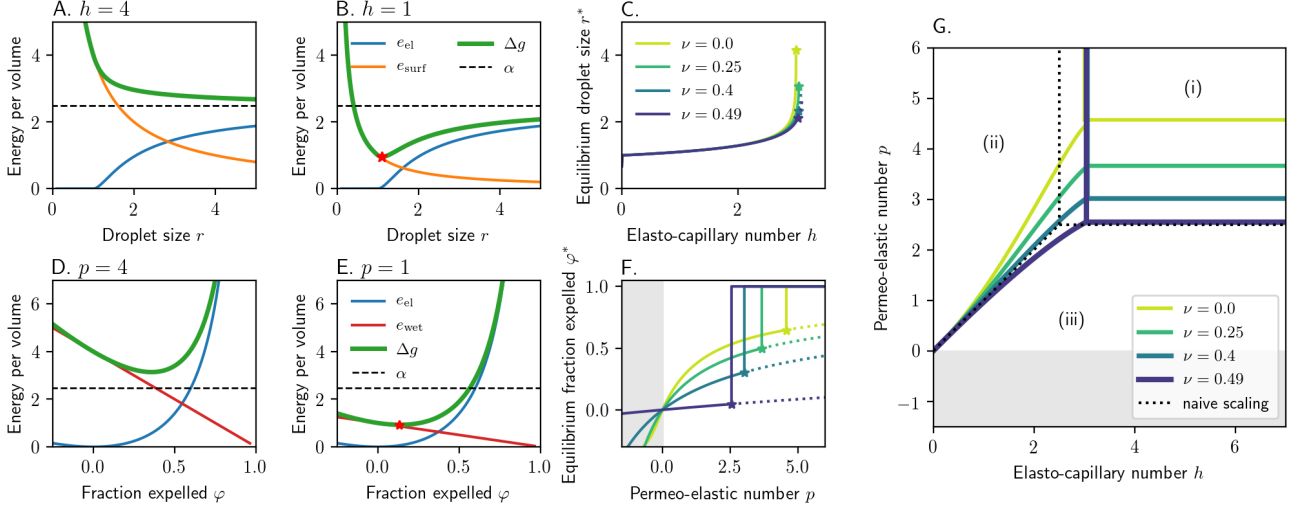


FIG. 3. Analysis of droplet phases within compressible NH networks. **A-B.** Elastic energy (blue, e_{el}), surface energy (orange, e_{surf}) and total free energy (green, $\Delta g = e_{el} + e_{surf}$) per volume for a droplet as a function of pore size r , respectively for elasto-capillary numbers $h = 4$ (showing monotonic decay of Δg) and $h = 1$ (showing a global minimum of Δg at r^* , red star). Dashed black line indicates the $\lambda \rightarrow \infty$ cavitated limit. **C.** Equilibrium pore size r^* as a function of the elasto-capillary number h , for different Poisson ratios ν of the network. Star indicates the limit of stability of phase (ii). **D-E.** Elastic, wetting (red, e_{wet}) and free energy (green, $\Delta g = e_{el} + e_{wet}$) per volume of a large droplet permeating through the network, as a function of the expelled volume fraction φ of the network, respectively for permeo-elastic numbers $p = 4$ (where cavitation is favored) and $p = 1$ (with global minimum at φ^* , red star). **F.** Equilibrium expelled volume fraction φ^* of the network as a function of the permeo-elastic number p . Dashed lines indicate metastable states, with cavitation ($\varphi^* = 1$) energetically favored. **G.** Phase diagram indicating the most stable phase in the (p, h) plane. Dotted lines indicate naive scaling results with $\alpha = 5/2$, as in Fig. 2. The shaded area in F,G indicate $p < 0$, i.e., a contractile droplet attracting the network. In A,B,D,E we take $\nu = 0.4$. Energy densities and length scales are respectively normalized by the linear shear modulus G and the pore size ξ .

interface through which the network permeates. In addition to a bulk energy term (Eq. (5)), network wetting can induce an effective change of liquid-liquid surface energy, in particular if filaments align with the interface. We do not consider such an effect in this article.

Again, in the spirit of a simple scaling analysis, we first neglect the network deformation in response to this stress and set $\varphi = 0$. The free energy per volume corresponding to this permeated scenario is thus

$$\Delta g_{(iii)} \sim \sigma_p. \quad (6)$$

Comparing this expression with Eq. (2), we find that the most stable phase is controlled by a second dimensionless quantity, namely the *permeo-elastic number*

$$p \equiv \frac{\sigma_p}{G}, \quad (7)$$

which is a measure of the degree of network deformation at the interface induced by the permeation stress. For $p > \alpha$, scenario (i) is the most stable: the repulsion between the network and the minority liquid is sufficiently strong to fully expel the network from the droplet, leading to cavitation. For $p < \alpha$, the droplet permeates through the network rather than excluding it, and scenario (iii) is preferred. Finally, when the elasto-capillary number $h < \alpha$, the phase boundary between scenarios (ii) and (iii) is given by the line $p = h$.

The results of this scaling analysis are summarized in a phase diagram in the (p, h) plane in Fig. 2, which predicts the most stable demixed phase. These phase boundaries depend only on the liquid and network properties, not on the degree of supersaturation: to assess whether demixing takes place or not, the free energy penalty of the most stable phase (Eq. 2, 3 or 6) should be added to the demixing free energy per volume in the absence of network. We note that for scenarios (i-ii), the network hinders phase separation and stabilizes the mixed phase; for scenario (iii), this depends on the sign of p : for $\sigma_p < 0$, the network prefers the minority phase and favors phase separation.

We have so far considered only the dominant contribution to the free energy for each scenario – either E_{el} , E_{surf} or E_{wet} . Network deformation will however occur in each of the three scenarios: in (ii), microdroplets exert a pressure on the network, while in (iii), a permeation stress $\sigma_p > 0$ results in a partial expulsion of the network from the droplet. To quantitatively predict the locations of the phase boundaries between scenarios and the nature of associated phase transitions, we next discuss the deformation behavior arising from an isolated droplet embedded within a slightly compressible NH network (see SI Secs. A-B).

Examining first scenarios (i-ii) for which the network is fully excluded from the droplet, we consider a droplet

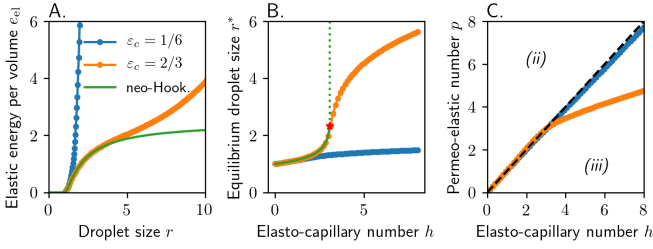


FIG. 4. Numerical analysis of strain-stiffening materials with the nonlinear contribution to the elastic energy density described by a term $\propto ((\lambda^2 - 1)/\epsilon_c)^3$ (see SI Sec. D), where λ is the stretch and the parameter ϵ_c controls the strength of nonlinearity. Low (blue) and high (orange) values of ϵ_c describe strong and weak nonlinearity, respectively. The analytical solution for non-stiffening NH materials is also shown (green). **A.** Elastic energy per droplet volume as a function of droplet size. **B.** Equilibrium droplet size r^* as a function of the elasto-capillary number h . For NH materials the cavitation transition is shown as a dotted line. **C.** Phase boundary between microdroplets (ii) and permeated (iii) phases. Cavitation (i) is suppressed by the strain-stiffening. Dashed line indicates naive scaling $p = h$.

of radius r in a spherical cavity of initial radius ξ that corresponds to the characteristic pore size of the network. When the elasto-capillary number h is large (Fig. 3A), the free energy per volume of the droplet $\Delta g = e_{el} + e_{surf}$ decreases monotonically with droplet size r , indicating that cavitation (scenario i) is thermodynamically favored. At small h (Fig. 3B), in contrast, the free energy exhibits a global minimum at $r^* \gtrsim \xi$, and size-limited microdroplets with radius r^* as per scenario (ii) are favored. For positive Poisson's ratios ν , the radius r^* increases sharply with the elasto-capillary number h (Fig. 3C), but remains finite up to the limit of stability of microdroplets, indicating that the cavitation transition ($i \rightarrow ii$) is weakly first-order as surface tension is increased or, equivalently, as the shear modulus of the network is reduced. Interestingly, this transition becomes continuous for auxetic materials with $\nu < 0$ (see SI Sec. C).

Turning now to the case of a permeated network with homogeneous stretch λ inside the droplet, we consider a macroscopic phase separated droplet (thus neglecting the surface energy e_{surf}) for which the free energy per volume is a function of the fraction $\varphi = 1 - \lambda^{-3}$ of the network expelled from the droplet. When the permeo-elastic number p is large, the free energy exceeds that of the cavitated case for all φ (Fig. 3D). In contrast, at small values of p (Fig. 3E) the global free energy density minimum occurs at a finite value φ^* , and permeation is favored. When p increases, the equilibrium expelled network fraction φ^* increases continuously up to the cavitation point, at which it experiences a compressibility-dependent jump (Fig. 3F), implying that the transition is discontinuous. We summarize these results in a phase diagram for NH materials (Fig. 3G).

While an NH constitutive law describes the deformation behavior of a broad class of materials at finite

stretches, many biomolecular networks differ by exhibiting nonlinear *strain-stiffening* behavior [21–23] whereby the (nominal) tensile stress grows faster than linearly with the stretch – either as a power-law with exponent > 1 , or with a divergence at finite stretch. In the permeated case, this nonlinearity limits the exclusion of the network from the droplet, with moderate effects on the phase stability. In contrast, strain stiffening strongly affects phases (i-ii) where the network is fully excluded: the free energy of the cavity grows asymptotically faster than its volume, and the elastic penalty $e_{el}(r)$ diverges in the limit of large droplets, as illustrated in Fig. 4A by numerical analysis of a minimal model for power-law strain stiffening materials (see SI Sec. D). As a consequence, effectively $\alpha \rightarrow \infty$, and scenario (i) is suppressed: the global energy minimum always occurs at a finite droplet radius r^* , leading to size selection, as recently noted in the context of the Gent model [24]. When the nonlinearity is strong, the equilibrium droplet size is $r^* \gtrsim \xi$ even at large capillary forces corresponding to $h \gg 1$ (Fig. 4B, blue), and microdroplets are stable when $p \gtrsim h$ (Fig. 4C). When the nonlinearity is weak and emerges only at large stretch, in contrast, microdroplets transition from being linearly arrested with size $r^* \gtrsim \xi$ at $h \lesssim 3$, to being non-linearly arrested at a mesoscopic, material dependent size $r^* \gg \xi$ at $h \gtrsim 3$ (Fig. 4, orange). This transition is a smooth crossover for realistic material parameters, and results in a change of slope in the phase boundary between microdroplets and permeated droplets as larger droplets incur a lower surface penalty (Fig. 4C).

In summary, we have shown that, upon accounting for the heterogeneity of the network and its nonlinear mechanical properties, as well as microscopic capillary forces responsible for network expulsion, a complex picture of liquid-liquid phase separation (LLPS) within an elastic network emerges. Specifically, in addition to the well-known cavitated macroscopic droplets which fully exclude the network, two other phases are thermodynamically possible: elastically limited microdroplets at the network pore scale, and network-including macroscopic droplets. We introduced two dimensionless parameters governing the relative stability of these morphologies: the elasto-capillary number h (Eq. (4)) and the permeo-elastic number p (Eq. (7)), and constructed a phase diagram in the (p, h) plane (Figs. 2, 3G and 4C) that quantifies the equilibrium droplet size and network deformation behavior.

Finally, we discuss the relevance of the predicted phases for experimental systems by providing the order-of-magnitude estimates for the relevant parameters, presented in Table I. For fluorinated oil demixing in silicone gels (system I with $h \gg \alpha$), consistently with experimental observations [9, 10, 12], only macroscopic phase separation appears to be relevant: these networks are too homogeneous, and the surface tension too high, to permit microphase separation. We note that an independent study proposes that a combination of mesh size heterogeneity, strongly heterogeneous nucleation at sparse loci,

TABLE I. Order-of-magnitude estimates of the shear modulus G , network mesh size ξ , surface tension ξ and permeation stress σ_p for three classes of experimental systems. We indicate the range of variation of the elasto-capillary number h and the permeo-elastic number p , and conclude on the plausible scenarios for LLPS (most likely in bold). Details in SI Sec. F.

System	G	ξ	γ	σ_p	h	p	Scenarios
I Oil in silicone gel	$10^3 - 3.10^5 \text{ Pa}$	$2 - 14 \text{ nm}$	$4 \times 10^{-3} \text{ N m}^{-1}$	$10^4 - 3.10^5 \text{ Pa}$	20-700	1.1 - 6.5	(i) , (iii)
II Cytoplasmic cond.	$10 - 100 \text{ Pa}$	$50 - 150 \text{ nm}$	10^{-6} N m^{-1}	$\pm 0.2 - 2 \text{ Pa}$	0.2-6	$\pm 10^{-3} - 0.2$	(ii) , (iii)
III Nuclear condensates	$10 - 10^3 \text{ Pa}$	$7 - 20 \text{ nm}$	$10^{-7} - 10^{-6} \text{ N m}^{-1}$	$\pm 10 - 100 \text{ Pa}$	0.01-10	$\pm 0.01 - 10$	(i) , (ii) , (iii)

and network fracture under stress could lead to the coexistence of microdroplets and cavitated droplets in these systems [16]. In contrast, for cytoplasmic condensates (system II), low surface tension, large mesh sizes and stiff filaments make permeation the most likely scenario, while cavitation appears to be ruled out by our theory: if droplets exclude the cytoskeleton, they are likely to be size-selected at the network mesh size. Finally, in the context of intracellular phase separation in the nucleoplasm (III), all three scenarios are plausible. In particular, we predict that mesh-size-selected microdroplets are possible in chromatin for biologically relevant parameters. Interestingly, the chromatin mesh size is well below the optical resolution limit: if such microdroplets exist, they are likely not to have been fully characterized yet. For instance, it was recently proposed that phase-separated condensates are involved in the activation and repression of gene transcription [25–27]. Our work suggests that such condensates might be elastically limited by the mechanisms presented herein.

We note that our key theoretical predictions rely on several important assumptions. First, we have focused on thermodynamic equilibrium states, neglecting both the kinetic pathways leading to them such as droplet ripening [10, 17, 18, 28] and merging [29] and, in the case of biological systems, their inherently out-of-equilibrium nature. Second, we have ignored all elastic interactions between the droplets, which is justifiable when the typical droplet separations are much greater than their size. Third, we have neglected all visco-elastic effects in the network: we thus considered systems over time scales long enough for phase separation to complete, yet short enough for the network to retain its mechanical integrity. Exploring the effects of network-mediated droplet inter-

actions and kinetic processes would provide additional insights into the behavior of elastically limited droplets, and is left for future work.

Our study also suggests new ways to engineer size-controlled microdroplets through elastic limitation. These could be useful for nanofabrication, as well as to serve as crucibles for chemical reactions favored by phase exchange: the very high surface-to-volume ratio would permit fast exchange between the two phases. The multi-stage chemical reactions can be guided in structured multi-phase droplets, such as is the case with the ribosome biogenesis in nucleoli [7], where the internal organization of phases is dictated by their surface tensions [30]. Finally, we note that while we have focused on the case of droplets that (partially) expel the network, our theory predicts that capillary forces are reversed when $p < 0$: in this case, the network facilitates phase separation and condenses around the droplets. This scenario may be involved in the formation of heterochromatin domains by phase separation of HP1a [31]. Such network-droplet attraction could also couple to the nonlinear mechanics of fiber networks to result in large-scale stresses [32, 33].

Acknowledgments. SM, AK and MPH are supported by NSF through the Princeton University Materials Research Science and Engineering Center DMR-2011750. P.R. is supported by the NSF through the Center for the Physics of Biological Function (PHY-1734030). The project leading to this publication has received funding from the “Investissements d’Avenir” French Government program managed by the French National Research Agency (ANR-16-CONV-0001) and from Excellence Initiative of Aix-Marseille University - A*MIDEX.

-
- [1] C. P. Brangwynne, C. R. Eckmann, D. S. Courson, A. Rybarska, C. Hoegge, J. Gharakhani, F. Jülicher, and A. A. Hyman, Germline P Granules Are Liquid Droplets That Localize by Controlled Dissolution/Condensation, *Science* **324**, 1729 (2009).
 - [2] S. Alberti, A. Gladfelter, and T. Mittag, Considerations and Challenges in Studying Liquid-Liquid Phase Separation and Biomolecular Condensates, *Cell* **176**, 419 (2019).
 - [3] A. A. Hyman, C. A. Weber, and F. Jülicher, Liquid-Liquid Phase Separation in Biology, *Annual Review of Cell and Developmental Biology* **30**, 39 (2014).
 - [4] J. Berry, C. P. Brangwynne, and M. Haataja, Physical principles of intracellular organization via active and passive phase transitions, *Reports on Progress in Physics* **81**, 046601 (2018).
 - [5] D. Bracha, M. T. Walls, and C. P. Brangwynne, Probing and engineering liquid-phase organelles, *Nature Biotechnology* **37**, 1435 (2019).
 - [6] J.-M. Choi, A. S. Holehouse, and R. V. Pappu, Physical Principles Underlying the Complex Biology of Intracellular Phase Transitions, *Annual Review of Biophysics* **49**, 107 (2020).
 - [7] M. Feric, N. Vaidya, T. S. Harmon, D. M. Mitrea, L. Zhu,

- T. M. Richardson, R. W. Kriwacki, R. V. Pappu, and C. P. Brangwynne, Coexisting liquid phases underlie nucleolar sub-compartments, *Cell* **165**, 1686 (2016).
- [8] Y. Shin, Y.-C. Chang, D. S. W. Lee, J. Berry, D. W. Sanders, P. Ronceray, N. S. Wingreen, M. Haataja, and C. P. Brangwynne, Liquid Nuclear Condensates Mechanically Sense and Restructure the Genome, *Cell* **175**, 1481 (2018).
- [9] R. W. Style, T. Sai, N. Fanelli, M. Ijavi, K. Smith-Mannschott, Q. Xu, L. A. Wilen, and E. R. Dufresne, Liquid-Liquid Phase Separation in an Elastic Network, *Physical Review X* **8**, 011028 (2018).
- [10] K. A. Rosowski, T. Sai, E. Vidal-Henriquez, D. Zwicker, R. W. Style, and E. R. Dufresne, Elastic ripening and inhibition of liquid-liquid phase separation, *Nature Physics* **16**, 422 (2020).
- [11] A. Semenov, Contribution to the theory of microphase layering in block-copolymer melts, *Journal of Experimental and Theoretical Physics* **88**, 733 (1984).
- [12] J. Y. Kim, Z. Liu, B. M. Weon, T. Cohen, C.-Y. Hui, E. R. Dufresne, and R. W. Style, Extreme cavity expansion in soft solids: Damage without fracture, *Science Advances* **6**, eaaz0418 (2020).
- [13] M. Kothari and T. Cohen, Effect of elasticity on phase separation in heterogeneous systems, *Journal of the Mechanics and Physics of Solids* **145**, 104153 (2020).
- [14] L. R. G. Treloar, *The Physics of Rubber Elasticity*, third edition ed., Oxford Classic Texts in the Physical Sciences (Oxford University Press, Oxford, New York, 2005).
- [15] S. Raayai-Ardakani, D. R. Earl, and T. Cohen, The intimate relationship between cavitation and fracture, *Soft Matter* **15**, 4999 (2019).
- [16] E. Vidal-Henriquez and D. Zwicker, Cavitation controls droplet sizes in elastic media, to appear (2021).
- [17] E. Vidal-Henriquez and D. Zwicker, Theory of droplet ripening in stiffness gradients, *Soft Matter* **16**, 5898 (2020).
- [18] K. Rosowski, E. Vidal-Henriquez, D. Zwicker, R. W. Style, and E. R. Dufresne, Elastic stresses reverse Ostwald ripening, *Soft Matter* **16**, 5892 (2020).
- [19] X. Shao, S. Fredericks, J. Saylor, and J. Bostwick, Elastocapillary Transition in Gel Drop Oscillations, *Physical Review Letters* **123**, 188002 (2019).
- [20] P. G. De Gennes, Liquid-liquid demixing inside a rigid network. Qualitative features, *The Journal of Physical Chemistry* **88**, 6469 (1984).
- [21] R. W. Ogden, *Non-linear Elastic Deformations* (Courier Corporation, 1997).
- [22] C. Storm, J. J. Pastore, F. C. MacKintosh, T. C. Lubensky, and P. A. Janmey, Nonlinear elasticity in biological gels, *Nature* **435**, 191 (2005).
- [23] K. A. Erk, K. J. Henderson, and K. R. Shull, Strain Stiffening in Synthetic and Biopolymer Networks, *Biomacromolecules* **11**, 1358 (2010).
- [24] X. Wei, J. Zhou, Y. Wang, and F. Meng, Modeling Elastically Mediated Liquid-Liquid Phase Separation, *Physical Review Letters* **125**, 268001 (2020).
- [25] W.-K. Cho, J.-H. Spille, M. Hecht, C. Lee, C. Li, V. Grube, and I. I. Cisse, Mediator and RNA polymerase II clusters associate in transcription-dependent condensates, *Science* **361**, 412 (2018).
- [26] B. R. Sabari, A. Dall'Agnese, A. Boija, I. A. Klein, E. L. Coffey, K. Shrinivas, B. J. Abraham, N. M. Hannett, A. V. Zamudio, J. C. Manteiga, C. H. Li, Y. E. Guo, D. S. Day, J. Schuijers, E. Vasile, S. Malik, D. Hnisz, T. I. Lee, I. I. Cisse, R. G. Roeder, P. A. Sharp, A. K. Chakraborty, and R. A. Young, Coactivator condensation at super-enhancers links phase separation and gene control, *Science* **361**, 10.1126/science.aar3958 (2018).
- [27] N. Treen, S. F. Shimobayashi, J. Eeftens, C. P. Brangwynne, and M. S. Levine, Regulation of gene expression by repression condensates during development, *bioRxiv*, 2020.03.03.975680 (2020).
- [28] Y. Zhang, D. S. W. Lee, Y. Meir, C. P. Brangwynne, and N. S. Wingreen, Mechanical frustration of phase separation in the cell nucleus by chromatin, *bioRxiv*, 2020.12.24.424222 (2020).
- [29] D. S. W. Lee, N. S. Wingreen, and C. P. Brangwynne, Chromatin mechanics dictates subdiffusion and coarsening dynamics of embedded condensates, *Nature Physics* **10.1038/s41567-020-01125-8** (2021).
- [30] S. Mao, M. S. Chakraverti-Wuerthwein, H. Gaudio, and A. Kosmrlj, Designing the Morphology of Separated Phases in Multicomponent Liquid Mixtures, *Physical Review Letters* **125**, 218003 (2020).
- [31] A. R. Strom, A. V. Emelyanov, M. Mir, D. V. Fyodorov, X. Darzacq, and G. H. Karpen, Phase separation drives heterochromatin domain formation, *Nature* **547**, 241 (2017).
- [32] P. Ronceray, C. P. Broedersz, and M. Lenz, Fiber networks amplify active stress, *Proceedings of the National Academy of Sciences* **113**, 2827 (2016).
- [33] P. Ronceray, C. P. Broedersz, and M. Lenz, Stress-dependent amplification of active forces in nonlinear elastic media, *Soft Matter* **15**, 331 (2019).
- [34] S. Biwa, Cavitation in finite elasticity with surface energy effects, *International Journal of Non-Linear Mechanics* **41**, 1084 (2006).
- [35] A. Meurer *et al.*, SymPy: symbolic computing in Python, *PeerJ Computer Science* **3**, e103 (2017).
- [36] C. O. Horgan and G. Saccomandi, A Molecular-Statistical Basis for the Gent Constitutive Model of Rubber Elasticity, *Journal of Elasticity* **68**, 167 (2002).
- [37] A. N. Gent, A New Constitutive Relation for Rubber, *Rubber Chemistry and Technology* **69**, 59 (1996).
- [38] E. M. Arruda and M. C. Boyce, A three-dimensional constitutive model for the large stretch behavior of rubber elastic materials, *Journal of the Mechanics and Physics of Solids* **41**, 389 (1993).
- [39] M. C. Boyce, Direct Comparison of the Gent and the Arruda-Boyce Constitutive Models of Rubber Elasticity, *Rubber Chemistry and Technology* **69**, 781 (1996).
- [40] P. Virtanen *et al.*, SciPy 1.0: fundamental algorithms for scientific computing in Python, *Nature Methods* **17**, 261 (2020).
- [41] A. F. Pegoraro, P. Janmey, and D. A. Weitz, Mechanical Properties of the Cytoskeleton and Cells, *Cold Spring Harbor Perspectives in Biology* **9**, a022038 (2017).
- [42] T. Hohmann and F. Dehghani, The Cytoskeleton - A Complex Interacting Meshwork, *Cells* **8**, 10.3390/cells8040362 (2019).

Liquid demixing in elastic networks: cavitation, permeation, or size selection?

Supplementary Information

Appendix A: Mathematical framework: modeling liquid droplets in an elastic network

We first discuss the framework we employ to assess the stability of each of the three scenarios considered in the main text: (i) cavitation, (ii) microdroplets, and (iii) permeation. Throughout this article, we consider a single spherical droplet of phase-separated liquid, in an infinite elastic medium representing the network. We thus neglect mechanical interactions between droplets, mediated by the network; this assumption is valid if the separation between droplets is much larger than their size (*i.e.* when the volume fraction of phase-separated droplets is small). The stability of each scenario is measured by the difference Δg of free energy per droplet volume, compared to an infinite droplet of phase separated liquid in the absence of an elastic network. This penalty is captured in three distinct terms: elastic energy stored in the network, liquid-liquid surface tension, and wetting energy. The latter two have closed forms as a function of the droplet size and inner stretch. The mathematically non-trivial aspect thus lies in the evaluation of the elastic energy resulting from the network deformation induced by the droplet.

We characterize the elastic medium by its *stored energy function* $W(\lambda_1, \lambda_2, \lambda_3)$ (which we leave unspecified for now), where the λ_i 's correspond to the three principal stretches. This function corresponds to the elastic energy density in the undeformed material coordinates. We consider a droplet of size r_d in a spherically symmetric infinite medium. We write the equilibrium deformation $r = r(R)$, such that a point at distance R from the droplet center in the initial undeformed state is displaced to radius $r(R)$ in the deformed state. In this geometry, the principal stretches are the radial stretch $\lambda_1(R) = \frac{dr}{dR} \equiv s$ and the hoop stretch $\lambda_2(R) = \lambda_3(R) = r/R \equiv t$.

We distinguish two geometries, depending on whether the network is excluded from the droplet (scenarios (i-ii)) or included (scenario (iii)):

- excluded network (Fig. 5A): the medium is modeled as an infinite material with an initial spherical pore of radius ξ in the reference configuration (left). A droplet of radius $r_d = r(\xi)$ stretches this pore by a factor $\lambda_d = r_d/\xi$ compared to this reference configuration (right). The elastic energy stored in the network outside the droplet is thus:

$$E_{\text{el,out}} = 4\pi \int_{\xi}^{\infty} W\left(\frac{dr}{dR}, \frac{r}{R}, \frac{r}{R}\right) R^2 dR \quad (\text{A1})$$

Introducing $u = R/\xi$, the radial stretch $s = dr/dR$ and the hoop stretch $t = r/R$, we obtain the following form for the elastic energy per unit volume of the droplet:

$$\frac{E_{\text{el,out}}}{v_d} = \frac{3}{\lambda_d^3} \int_1^{\infty} W(s(u), t(u), t(u)) u^2 du \equiv f_{\text{out}}(\lambda_d) \quad (\text{A2})$$

where $v_d = \frac{4}{3}\pi r_d^3$ is the droplet volume. Eq. (A2) should be minimized over the deformation field $t(u)$, with boundary condition $t(u=1) = \lambda_d$.

- included (permeated) network (Fig. 5B): the medium is modeled as an intact infinite material, and the pores are considered to be infinitesimally small. The droplet of radius r_d is placed at the center, and imposes a stress discontinuity at its surface. The material inside the droplet is isotropically and homogeneously deformed with stretch λ_i . The material outside the droplet is deformed in a similar way as previously, and hence the total elastic energy reads

$$E_{\text{el}} = E_{\text{el,in}} + E_{\text{el,out}} = \frac{4}{3}\pi \left(\frac{r_d}{\lambda_i}\right)^3 W(\lambda_i, \lambda_i, \lambda_i) + 4\pi \int_{r_d/\lambda_i}^{\infty} W\left(\frac{dr}{dR}, \frac{r}{R}, \frac{r}{R}\right) R^2 dR \quad (\text{A3})$$

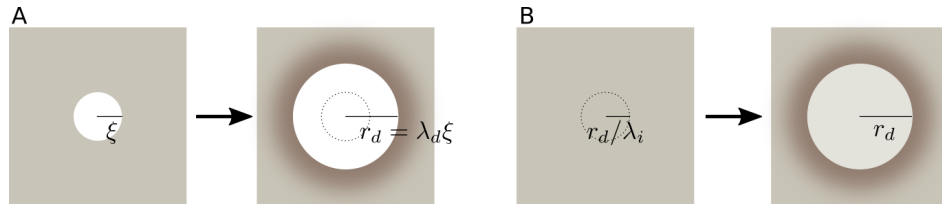


FIG. 5. Geometries of droplets considered here. **A.** Network exclusion, starting from a pore of size ξ stretched by a factor λ_d . **B.** Permeation of the droplet through the network, with network stretch λ_i inside the droplet.

which, divided by the droplet volume, is:

$$\frac{E_{\text{el}}}{v_d} = \frac{1}{\lambda_i^3} W(\lambda_i, \lambda_i, \lambda_i) + f_{\text{out}}(\lambda_i) \quad (\text{A4})$$

where f_{out} was defined in Eq. (A2). In this geometry, the fraction of the network excluded from the droplet is $\varphi = 1 - \lambda_i^{-3}$, so that the wetting energy reads $E_{\text{wet}} = v_d \sigma_p \lambda_i^{-3}$.

We finally recapitulate our definition of the free energy for each of the three phases considered in this article.

- Cavitation (*i*): the only contribution to the free energy is the elastic penalty, in the infinite-stretch limit of Eq. (A2):

$$\Delta g_{(i)} = \lim_{\lambda_d \rightarrow \infty} f_{\text{out}}(\lambda_d). \quad (\text{A5})$$

- Microdroplets (*ii*): we combine the elastic energy with network exclusion (Eq. (A2)) with the surface tension. The free energy is found by minimizing over the pore stretch (*i.e.* over the droplet radius):

$$\Delta g_{(ii)} = \min_{\lambda_d} \left[\frac{3\gamma}{\lambda_d \xi} + f_{\text{out}}(\lambda_d) \right] \quad (\text{A6})$$

where γ is the surface tension. Note that the minimization does not always yield a finite value for λ_d .

- Permeation (*iii*): we combine the elastic energy with network inclusion (Eq. (A4)) with the wetting energy. The free energy is found by minimizing over the pore stretch (*i.e.* over the excluded fraction of the network):

$$\Delta g_{(iii)} = \min_{\lambda_i} \left[\frac{\sigma_p + W(\lambda_i, \lambda_i, \lambda_i)}{\lambda_i^3} + f_{\text{out}}(\lambda_i) \right] \quad (\text{A7})$$

where σ_p is the permeation stress.

The mathematically non-trivial part, in all three scenarios, is the evaluation of the outer elastic energy density $f_{\text{out}}(\lambda)$. We combine two approaches, depending on the class of materials considered, *i.e.* on the functional form of W . In the case of neo-Hookean materials, we consider slightly compressible systems, which allows us to solve for the deformation field analytically, as discussed in Sec. B (corresponding to the results presented in Fig. 3 of the main text). For strain-stiffening materials (Fig. 4 of the main text), such an analytical approach is not possible, and we resort to a numerical estimation of f_{out} , as presented in Sec. D. In all cases, the free energy minimization over the value of λ in Eqs. (A6) and (A7) is then performed numerically.

Appendix B: Analytical treatment of slightly compressible neo-Hookean materials

Consider Eq. (A1), written in terms of arbitrary inner and outer radii R_{min} and R_{max} : $E_{\text{el,out}} = \int_{R_{\text{min}}}^{R_{\text{max}}} 4\pi R^2 W(\lambda_1, \lambda_2, \lambda_2) dR$. In mechanical equilibrium, $E_{\text{el,out}}$ is a minimum. Thus, the equilibrium deformation $r = r(R)$ can be obtained from a variational principle as

$$\frac{\delta E_{\text{el,out}}}{\delta r(R)} = 8\pi R \frac{\partial W}{\partial \lambda_2} - 4\pi \frac{d}{dR} \left(R^2 \frac{\partial W}{\partial \lambda_1} \right) = 0, \quad (\text{B1})$$

or

$$\frac{d}{dR} (R^2 W_1) - 2R W_2 = 0, \quad (\text{B2})$$

where $W_i \equiv \partial W / \partial \lambda_i$. [Note that here we assume that the system is compressible. In an incompressible system, the deformation is explicitly determined from $J = \frac{dr}{dR} \left(\frac{r}{R} \right)^2 = 1 \leftrightarrow \frac{dr}{dR} = \left(\frac{r}{R} \right)^{-2}$.] It is straightforward to show that $dW_1/dR = W_{11}r''(R) + 2W_{12}(r'(R)/R - r/R^2)$, where $W_{1j} \equiv \partial^2 W / \partial \lambda_1 \partial \lambda_j$. Upon introducing the hoop and radial stretches as $t = r(R)/R$ and $s(t) = dr/dR$, respectively, it can be shown that $r''(R) = ds/dR = ds/dt (s - t)/R$ and $dW_1/dR = W_{11}[ds/dt (s - t)/R] + 2W_{12}[s - t]/R$. Thus, Eq. (B2) becomes

$$W_{11} \frac{ds}{dt} = -2 \left(\frac{W_1 - W_2}{s - t} + W_{12} \right). \quad (\text{B3})$$

Let us next focus on the following simple form for the stored energy function W , corresponding to a slightly compressible neo-Hookean network [34]:

$$W(\lambda_1, \lambda_2, \lambda_3) = \frac{G}{2} \left[\lambda_1^2 + \lambda_2^2 + \lambda_3^2 - 3 - 2(\lambda_1 \lambda_2 \lambda_3 - 1) + \beta (\lambda_1 \lambda_2 \lambda_3 - 1)^2 \right], \quad (\text{B4})$$

with G and $\nu = (1 - \beta^{-1})/2$ denoting the shear modulus and Poisson's ratio, respectively. It is straightforward to show that, with this choice for W , Eq. (B3) becomes

$$(1 + \beta t^4) \frac{ds}{dt} = -2(1 + \beta s t^3). \quad (\text{B5})$$

The exact solution of Eq. (B5) is given by [34]

$$s(t) = \frac{C_0 - \Psi(t)}{\sqrt{1 + \beta t^4}}, \quad (\text{B6})$$

where C_0 denotes an integration constant, and

$$\frac{d\Psi(t)}{dt} = \frac{2}{\sqrt{1 + \beta t^4}} \quad \leftrightarrow \quad \Psi(t) = \int_{t_0}^t d\tau \frac{2}{\sqrt{1 + \beta \tau^4}}. \quad (\text{B7})$$

Now, consider the case where we have an initial pore of radius ξ embedded within an infinite elastic, neo-Hookean matrix, and the pore walls are subjected to a constant pressure p_0 . Far from the cavity, the matrix remains deformation-free, and hence $\lim_{t \rightarrow 1} s(t) = 1$. From the exact solution we immediately obtain

$$s_I(t) = \frac{\sqrt{1 + \beta} - \int_1^t d\tau \frac{2}{\sqrt{1 + \beta \tau^4}}}{\sqrt{1 + \beta t^4}}. \quad (\text{B8})$$

Now, consider subjecting the boundary of the pore to a stretch λ such that $r(\xi) = \lambda \xi$. The corresponding radial stretch is given by

$$s_I(\lambda) \equiv \Delta_I = \frac{\sqrt{1 + \beta} - \int_1^\lambda d\tau \frac{2}{\sqrt{1 + \beta \tau^4}}}{\sqrt{1 + \beta \lambda^4}}. \quad (\text{B9})$$

Now, the pressure p_0 required to sustain the deformation is given by

$$\frac{p_0(\lambda, \beta)}{G} = -\frac{W_1}{G\lambda^2} = 1 - \frac{\Delta_I}{\lambda^2} - \beta (\Delta_I \lambda^2 - 1). \quad (\text{B10})$$

We obtain the stored elastic energy as the total work of pressure forces from the undeformed state:

$$E_{\text{el, out}}(\lambda) = 4\pi\xi^3 \int_1^\lambda p_0(\lambda', \beta) \lambda'^2 d\lambda' \quad (\text{B11})$$

Using the formal calculus software SymPy [35] to expand the integral in Eq. (B9) in powers of β^{-1} (*i.e.* a weakly compressible expansion), we finally obtain the following expression for the elastic energy per droplet volume f_{out} as a function of the droplet stretch $\lambda = r/\xi$:

$$\begin{aligned} \frac{f_{\text{out}}(\lambda)}{G} = & + \frac{5}{2} - \frac{3}{\lambda} - \frac{1}{\lambda^3} + \frac{3}{2\lambda^4} \\ & + \beta^{-1} \left[-\frac{3}{40} + \frac{6}{5\lambda^3} - \frac{9}{4\lambda^4} + \frac{6}{5\lambda^5} - \frac{3}{40\lambda^8} \right] \\ & + \beta^{-2} \left[\frac{1}{48} - \frac{2}{15\lambda^3} + \frac{9}{80\lambda^4} + \frac{9}{80\lambda^8} - \frac{2}{15\lambda^9} + \frac{1}{48\lambda^{12}} \right] \\ & + \beta^{-3} \left[-\frac{15}{1664} + \frac{14}{325\lambda^3} - \frac{1}{32\lambda^4} - \frac{9}{1600\lambda^8} - \frac{1}{32\lambda^{12}} + \frac{14}{325\lambda^{13}} - \frac{15}{1664\lambda^{16}} \right] \\ & + \beta^{-4} \left[\frac{21}{4352} - \frac{22}{1105\lambda^3} + \frac{45}{3328\lambda^4} + \frac{1}{640\lambda^8} + \frac{1}{640\lambda^{12}} + \frac{45}{3328\lambda^{16}} - \frac{22}{1105\lambda^{17}} + \frac{21}{4352\lambda^{20}} \right] \\ & + \beta^{-5} \left[-\frac{3}{1024} + \frac{22}{1989\lambda^3} - \frac{63}{8704\lambda^4} - \frac{9}{13312\lambda^8} - \frac{1}{2304\lambda^{12}} - \frac{9}{13312\lambda^{16}} - \frac{63}{8704\lambda^{20}} + \frac{22}{1989\lambda^{21}} - \frac{3}{1024\lambda^{24}} \right] \\ & + O(\beta^{-6}) \end{aligned} \quad (\text{B12})$$

which we use to assess the stability of each phase, as described in Sec. A. For $\nu > 0$ (corresponding to $\beta > 1$ this expansion converges rapidly, and the results are essentially unaffected by including additional terms (in practice, for the results presented in Fig. 3 of the main text, we expand up to β^{-8}). In particular, we can read out the $\lambda \rightarrow \infty$ limit, corresponding to the cavitated free energy (Eq. (A5)):

$$\alpha \equiv \frac{\Delta g_{(i)}}{G} = \frac{1}{G} \lim_{\lambda \rightarrow \infty} f_{\text{out}}(\lambda) = \frac{5}{2} - \frac{3}{40\beta} + \frac{1}{48\beta^2} - \frac{15}{1664\beta^3} + \frac{21}{4352\beta^4} - \frac{3}{1024\beta^5} + \frac{99}{51200\beta^6} + O(\beta^{-7}) \quad (\text{B13})$$

Note that we also have $\alpha = p_0^*/G$, where p_0^* is the cavitation pressure. As expected, in the limit $\beta \rightarrow \infty$, $p_0^*/G \rightarrow 5/2$, in agreement with the classic cavitation result for incompressible neo-Hookean materials. For reasonable values of $\nu = 1/3$ ($\beta = 3$) or $\nu = 1/4$ ($\beta = 2$), Eq. (B13) yields $p_0^*/G \approx 2.48$ and 2.47, respectively. Finite compressibility thus reduces the critical cavitation pressure, albeit to a rather small degree. We also note that for the special case $\beta = 1$ (corresponding to $\nu = 0$), $p_0^*/G = 2 - \sqrt{2} + 4/\sqrt{\pi} \Gamma^2(5/4) \approx 2.44$, where $\Gamma(x)$ denotes the Euler gamma function, while the series approximation in Eq. (B13) yields $p_0^*/G \approx 2.44$, in excellent agreement with the exact result. Cavitation pressures for several representative compressibilities are listed in Table 1.

β	1	2	3	5	10	50	∞
ν	0	1/4	1/3	0.4	0.45	0.49	1/2
$\alpha = p_0^*(\beta)/G$	2.439	2.467	2.477	2.486	2.493	2.4985	5/2

TABLE II. Critical cavitation pressure of a finite spherical pore in an infinite, slightly compressible Neo-Hookean matrix at varying compressibilities.

Appendix C: Limit of metastability of microdroplets in the neo-Hookean model

We investigate here the nature of the equilibrium transition between microdroplets (scenario *ii*) and cavitation (scenario *i*), which is controlled by the elasto-capillary number h . To this aim, it is useful to consider the free energy per volume of a droplet of size $r = \lambda\xi$ as a function of its stretch λ , in the large λ limit that can be read out from Eq. (B12):

$$\frac{1}{G} \Delta g(\lambda) = \alpha(\beta) + \frac{h-3}{\lambda} + \frac{A_3(\beta)}{\lambda^3} + O(\lambda^{-4}) \quad (\text{C1})$$

where again $\beta = 1/(1-2\nu)$ is the compressibility parameter, and $A_3(\beta)$ is the coefficient of the inverse cubic term. Interestingly, the leading order in the expansion changes sign when $h = 3$ (independently of β), and around this value the free energy is thus dominated by higher-order terms. Depending on the compressibility, we identify two qualitatively distinct behaviors when varying h , as shown in Fig. 6:

- for $\nu > 0$, *i.e.* for usual materials, we have the following sequence of regimes:
 - $h < 3$: $\Delta g(\lambda)$ exhibits a single minimum at a finite $\lambda^* = r^*/\xi$, corresponding to the microdroplets scenario. Near equilibrium, droplets larger than r^* would shrink (“anti-ripen”) so as to reach the equilibrium size.
 - $3 < h < h_c$: microdroplets are the global free energy minimum, but there is a local maximum at $\lambda > \lambda^*$. As a result, $\lambda = \infty$ is a local minimum of free energy, and cavitated droplets are metastable.
 - $h_c < h < h^\dagger$: the global minimum of free energy is at $\lambda = \infty$, and cavitation is the stable scenario; however, a local minimum exists at r^\dagger , corresponding to metastable microdroplets.
 - $h > h^\dagger$: the free energy is monotonically decreasing as a function of λ , cavitation is stable and there exists no metastable state.

The transition between scenarios (*i*) and (*ii*) governed by h is thus first-order. However, plotting in Fig. 7 the values of h_c and h^\dagger over the physical range of Poisson’s ratio values ν , we note that the range of metastability corresponding to this first-order transition is very narrow, and restricted to values $3 < h < 3.11$ for all ν .

- for $\nu < 0$, *i.e.* for auxetic materials, we observe a second-order transition between scenarios (*i*) and (*ii*) (right panels in Fig. 6), with a continuous divergence of the droplet radius as $r^* \sim (3-h)^{-1/2}$ as $h \rightarrow 3$.

Overall, this analysis shows that at $\nu > 0$ the cavitation transition is *weakly first order*, characterized by the proximity to a critical point at $\nu = 0$, sharp increase of the droplet size near the transition (as shown in Fig 3C of the main text), and very limited range of metastability.

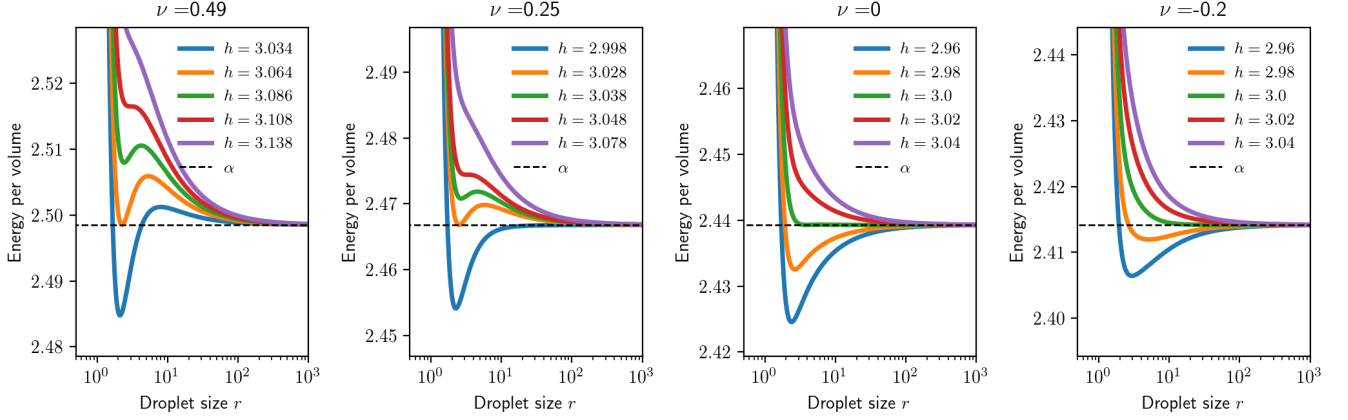


FIG. 6. Plots of $\frac{1}{G}\Delta g(\lambda)$ for different values of h and ν . The metastability regimes corresponding to a first-order transition are apparent for $\nu > 0$ (left two panels, with the equilibrium transition $h = h_c$ in orange and the end of metastability $h = h^\dagger$ in red). For $\nu \leq 0$ (right two panels), the transition is second-order and occurs at $h = 3$.

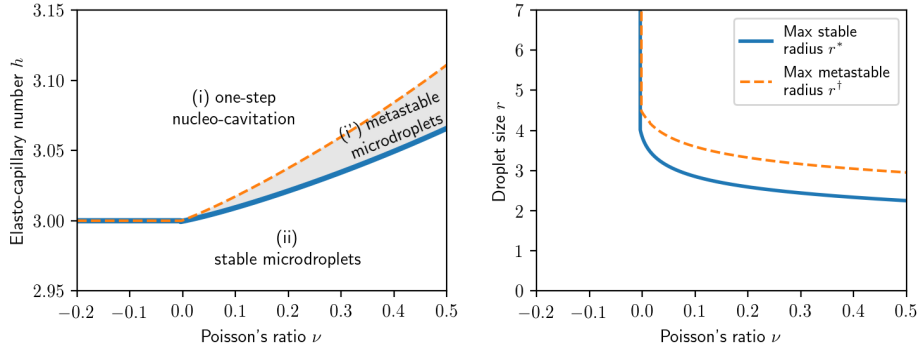


FIG. 7. Left: equilibrium transition line h_c (solid blue line) and metastability limit h^\dagger (dashed orange line) as a function of Poisson's ratio ν . The shaded area indicates the region in which microdroplets can be metastable. Note the very limited range of h values represented here. Right: maximum radius for stable microdroplets (solid blue line) and metastable droplets (dashed orange line). At $\nu < 0$ these are infinite, as the cavitation transition is continuous.

Appendix D: Minimal model for strain-stiffening effects

The stored energy function W for neo-Hookean materials [14] in Eq. (B4) does not capture strain-stiffening effects occurring in macromolecular systems at large stretches [21, 36–39]. To account for such effects, we consider the following modified stored energy function:

$$W = \frac{G}{2} \left[(I_1 - 3) - 2(J - 1) + \beta(J - 1)^2 + \left(\frac{I_1 - 3}{6\varepsilon_c} \right)^3 \right], \quad (\text{D1})$$

where $I_1 = \lambda_1^2 + \lambda_2^2 + \lambda_3^2$ and $J = \lambda_1\lambda_2\lambda_3$, and where ε_c denotes a characteristic strain at which stiffening effects become significant. It should be noted that the last term in Eq. (D1) emerges as the leading order term in a polynomial expansion of the classic Arruda-Boyce [38, 39] and Gent [37] models for large-stretch behavior of polymer systems.

The above choice for W is both convenient and physically-based: (1) At infinitesimally small strains, $W \sim G \left[\epsilon_{ij}\epsilon_{ij} + \frac{\nu}{1-2\nu}\epsilon_{ii}\epsilon_{jj} \right]$, in accordance with linear elasticity theory, where $\beta^{-1} = (1-2\nu)$ with ν denoting the Poisson's ratio and ϵ the linear strain. (2) By taking $\varepsilon_c \rightarrow \infty$, we recover the (slightly) compressible neo-Hookean model in Eq. (B4). (3) Asymptotically, $W \sim [(I_1 - 3)/(6\varepsilon_c)]^3 \sim [(\lambda_{chain}^2 - 1)/(2\varepsilon_c)]^3$, indicating a strong stiffening effect when $I_1 \rightarrow (3 + 6\varepsilon_c)$. Therefore, this form of W can be viewed as a minimal model for slightly compressible, strain-stiffening hyperelastic materials. Specifically, by tuning the parameter β , we can vary the compressibility with $\beta \rightarrow \infty$ corre-

sponding to a perfectly incompressible material, while by tuning ε_c , we can vary the material response from weakly stiffening (large ε_c) to strongly stiffening (small ε_c).

We employ numerical simulations to study the influence of strain-stiffening of the network on liquid-liquid phase separation. Specifically, to evaluate $f_{\text{out}}(\lambda)$ (as given by Eq. (A2)), we discretize the displacement field over an uneven grid, $u = [1, 1.16, 1.33, 1.51, \dots, 28.4, 29.2, u_{\text{max}} = 30]$ (with regular spacing of the values of \sqrt{u}). We evaluate the integral $\int_1^{u_{\text{max}}} W(s(u), t(u), t(u)) u^2 du$ using finite differences of the displacement field, and use the SciPy optimization package [40] (`scipy.optimize.minimize`) to perform the multivariate minimization of the energy of the displacement field, under the constraint $r(u = 1) = \lambda$. The outcome of this optimization is insensitive to the details of the discretization, and recovers the analytical solution presented in Sec. B in the case of neo-Hookean materials. We then pipe the resulting function $f_{\text{out}}(\lambda)$ into the free energy minimization described in Eqs. (A6)-(A7).

Appendix E: Further discussion of permeation stress σ_p .

We now discuss the microscopic origin of the permeation stress σ_p , and how it could be measured in practice. This term stems from the difference of wettability between the two liquids and the network. Microscopically, we can model the filaments composing the network as cylinders of radius r_f , corresponding to a liquid-solid interface area per unit length of $2\pi r_f$. Taking the filaments immersed in the majority liquid (liquid 1) as the reference of energy, the interfacial energy per unit length of a filament immersed in liquid 2 is thus $2\pi r_f(\gamma_{2S} - \gamma_{1S})$ where γ_{1S} and γ_{2S} respectively correspond to the interfacial energy between the network and liquids 1 and 2 (note that these interfacial energies are defined at the microscopic level, not at the network level). Denoting by ρ the volume fraction of the network in its rest state (we typically consider cases where $\rho \ll 1$), the liquid-network contact area per unit volume is $2\rho/r_f$. The difference of energy per unit volume between the network immersed in liquid 1 and in liquid 2 is thus:

$$\sigma_p = \frac{2}{r_f} \rho (\gamma_{2S} - \gamma_{1S}). \quad (\text{E1})$$

In the presence of strain in the network, its volume fraction may change: denoting by $\varphi = 1 - 1/(\lambda_1 \lambda_2 \lambda_3)$ the fraction of the network that is expelled compared to the undeformed state (where the λ_i 's are principal stretches), the energy per volume associated with immersing the stretched network into the minority liquid is thus $(1 - \varphi)\sigma_p$, corresponding to Eq. 5 of the main text.

At the liquid-liquid interface, the difference in surface energy results in a capillary force $F_c \sim 2\pi r_f(\gamma_{2S} - \gamma_{1S})$ on each filament going through the interface. At the network scale, this implies a stress discontinuity in the network: the network is being “sucked in” by the best-wetting liquid. Note that while Eq. (E1) relies on microscopic modeling of the network and applicability of the surface energy at the level of individual filaments, this stress discontinuity suggests that σ_p could also be measured experimentally, in a way that is independent from microscopic models. Indeed, consider a tube separating two chambers containing respectively liquids 1 and 2, with a cork of clamped network in the tube. Then σ_p corresponds to the pressure difference one must impose between the two chambers, so that the liquid-liquid interface remains steady within the network cork. This provides an experimentally viable way to measure σ_p . The existence and microscopic origin of this term was previously noted by de Gennes in the context of non-deformable porous media [20].

Note that in addition to the difference of liquid-solid surface energy, it is possible that the rest state of the network changes when immersed in liquid 2 – either swelling or shrinking – and thus that permeation induces a spontaneous strain in the network. This qualitatively distinct effect has, in practice, consequences similar to the effect discussed above, and thus simply results in a modification of σ_p for our purposes.

Appendix F: Estimation of physical parameters.

Here we discuss how we obtain the experimental values of parameters presented in Table I of the main text, for each of the three classes of systems considered. We focus on obtaining order-of-magnitude estimates for the two dimensionless parameters introduced in the main text: the elasto-capillary number $h \equiv 3\gamma/\xi G$ with γ the liquid-liquid surface tension, ξ the network pore size, and G the network shear modulus; and the permeo-elastic number $p \equiv \sigma_p/G$ with σ_p the permeation stress. Note that values of σ_p have not been reported in the literature, to the best of our knowledge; for this reason, we employ Eq. (E1) with typical values for surface tensions to get order-of-magnitude estimates of its range of variation. To this end, we substitute $\rho \approx r_f^2/\xi^2$, with r_f denoting the radius of the filaments constituting the network. Below, we consider three distinct systems, one synthetic, and two biological ones.

System I comprises the demixing of fluorinated oil embedded in a silicone gel, studied in great detail in Refs. [9, 10, 12]. The elastic modulus G is in the range 1.4 – 280kPa (we employ a Poisson ratio $\nu = 0.5$ to convert from

reported values of the Young's modulus). Following Ref. [10], we relate the modulus of this polymer network to its mesh size ξ through $\xi \sim (k_B T / G)^{1/3}$ with $k_B T = 4 \times 10^{-21} \text{J}$ the thermal energy. Hence, $\xi \sim 2.4 - 14 \text{nm}$. As for the surface tension, we employ $\gamma \approx 4.4 \text{mN m}^{-1}$, as reported in Ref. [12]. We take a representative molecular radius $r_f \approx 0.2 \text{nm}$ for PDMS chains, which yields $\sigma_p \sim 9 - 300 \text{kPa}$ (we emphasize that this is a rough estimate). The value $\alpha \approx 1.5$ (as the ratio between cavitation pressure and shear modulus) is reported in Ref. [9]. We conclude that the range of variation of dimensionless parameters h for system I is $h \sim 20 - 700 \gg \alpha$ and $p \sim 1.1 - 6.5 \gtrsim \alpha$, where larger values of h and p both correspond to softer gels. Our theory thus predicts that the relevant regime is predominantly cavitation (scenario *i*), with permeation (*iii*) being marginally possible for very stiff gels. This is consistent with the experimental observation of large, micron-sized droplets (while the mesh size is in the nanometer range) that fully exclude the surrounding network, as characterized by coherent anti-Stokes Raman scattering [12].

System III generally encompasses liquid condensates found in the nucleus of eukaryotic cells and mechanically interacting with the chromatin network, both native (such as nucleoli [7]) and biomimetic (such as CasDrop optogenetically activated condensates [8]). Due to the broad class of systems considered and to the scarcity of available quantitative data for physical parameters, we report only conservative ranges for our estimates. Following Ref. [8], we estimate the elastic modulus to be in the range $G \sim 10 - 1000 \text{Pa}$ and a mesh size $\xi \sim 7 - 20 \text{nm}$, with larger mesh sizes corresponding to softer chromatin. We estimate the surface tension to be in the range $\gamma \sim 10^{-7} - 10^{-6} \text{N m}^{-1}$. Indeed, such low values of surface tension have been reported for nucleolar proteins, $\gamma \sim 4 \times 10^{-7} \text{N m}^{-1}$ [7]. We take a radius $r_f = 1 \text{nm}$ for DNA, and a volume fraction $\rho \sim 0.1 - 0.4$ [8], which yields $\sigma_p \sim \pm 10 - 100 \text{Pa}$ (note that the sign of σ_p depends on whether the nucleoplasm or the liquid condensate better wets the chromatin, which is not known *a priori*). No value of α has been reported to our knowledge, and so we take $\alpha \sim 2.5$, corresponding to the neo-Hookean case, as a default. This results in a very broad range of possible values for dimensionless parameters, $h \sim 10^{-2} - 10$ and $p \sim \pm 10^{-2} - 10$. In particular, all three scenarios appear to be plausible: cavitation (*i*) in soft chromatin and for rather large values of the surface tension; nanodroplets confined at the mesh size (*ii*) if chromatin is stiffer and for low liquid-liquid surface tension; and finally permeation (*iii*) if the interfacial energy between chromatin and the condensate is low. Interestingly, only scenario (*i*) has been characterized yet: both nucleoli and engineered condensates form micron-sized droplets that have been shown to exclude the surrounding chromatin as they grow [8]. However, it is possible that mesh-size-level droplets actually exist, but have not been characterized yet as they would be significantly below optical resolution.

System II, finally, encompasses cytoplasmic liquid condensates such as stress granules and P-bodies, which interact mechanically with cytoskeletal networks, in particular the actin cortex. The main changes compared to system I are the properties of the elastic network. Reported values for the shear modulus of the cytoskeleton in intracellular conditions are similar in range to the nucleus, $G \sim 10 - 100 \text{Pa}$ [41]. However, the mesh size of the actin cortex, $\xi \sim 50 - 150 \text{nm}$ [42], is much larger than that of chromatin, as it is composed of sparser, stiffer filaments. We take a radius $r_f \sim 2.5 \text{nm}$ for F-actin filaments. Ref. [1] reports a surface tension $\gamma \approx 1 \mu\text{N m}^{-1}$ for cytoplasmic P-granules. The permeation stress is thus $\sigma_p \sim 0.2 - 2 \text{Pa}$. The range for dimensionless parameters is thus $h \sim 0.2 - 6$ and $p \sim \pm 10^{-3} - 0.2$. Interestingly, this excludes cavitation (*i*): permeation (*iii*) is the predominant scenario, while microdroplets (*ii*) remain marginally possible. It is therefore an open question whether permeation actually occurs in experiments.